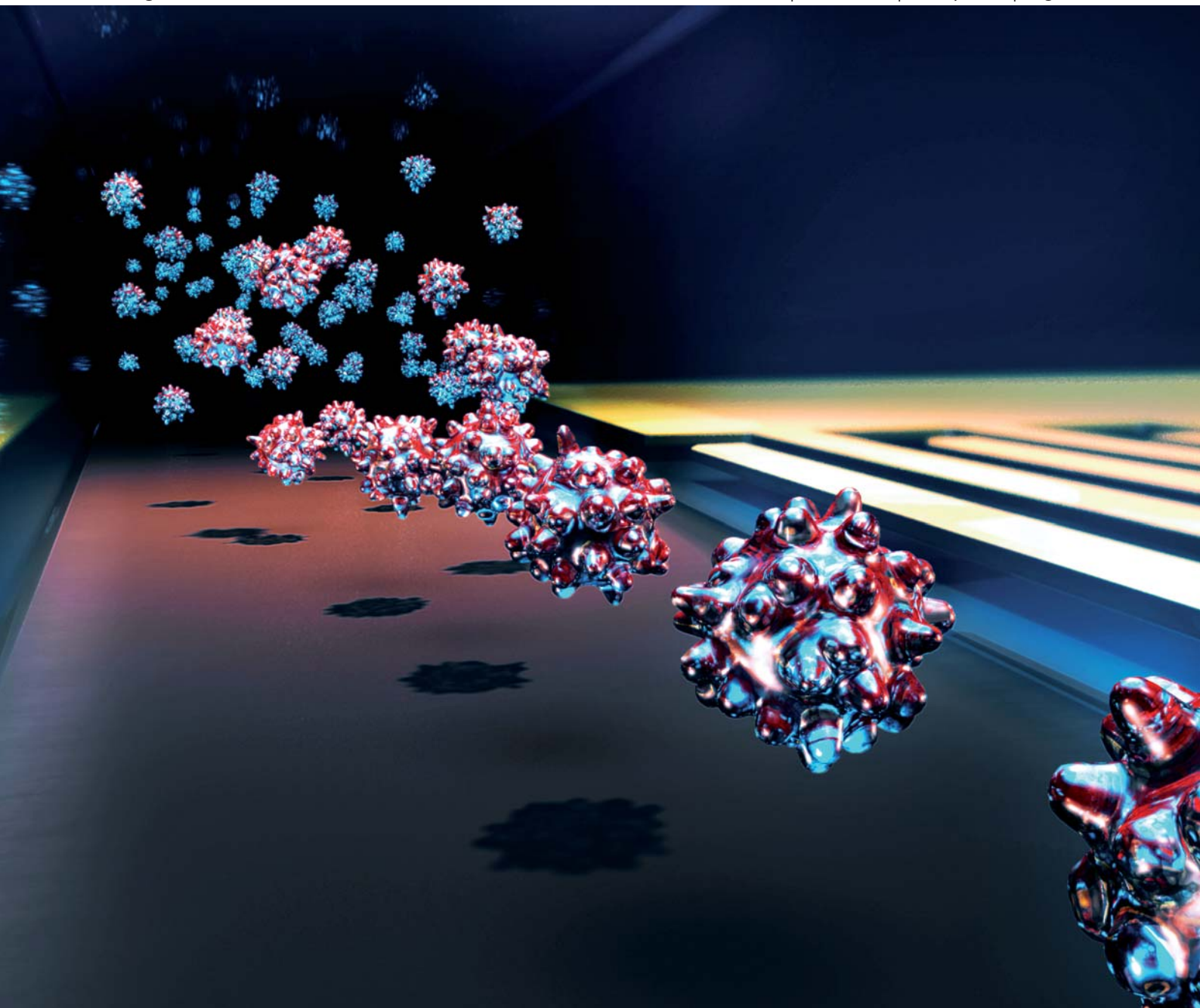


Lab on a Chip

Micro- & nano- fluidic research for chemistry, physics, biology, & bioengineering

www.rsc.org/loc

Volume 11 | Number 14 | 21 July 2011 | Pages 2297–2468



ISSN 1473-0197

RSC Publishing

PAPER

Tony Jun Huang *et al.*

Three-dimensional continuous particle focusing in a microfluidic channel via standing surface acoustic waves (SSAW)

Cite this: *Lab Chip*, 2011, **11**, 2319

www.rsc.org/loc

PAPER

Three-dimensional continuous particle focusing in a microfluidic channel *via* standing surface acoustic waves (SSAW)[†]

Jinjie Shi,^{ab} Shahrzad Yazdi,^{ac} Sz-Chin Steven Lin,^a Xiaoyun Ding,^a I-Kao Chiang,^a Kendra Sharp^d and Tony Jun Huang^{*a}

Received 15th January 2011, Accepted 17th May 2011

DOI: 10.1039/c1lc20042a

Three-dimensional (3D) continuous microparticle focusing has been achieved in a single-layer polydimethylsiloxane (PDMS) microfluidic channel using a standing surface acoustic wave (SSAW). The SSAW was generated by the interference of two identical surface acoustic waves (SAWs) created by two parallel interdigital transducers (IDTs) on a piezoelectric substrate with a microchannel precisely bonded between them. To understand the working principle of the SSAW-based 3D focusing and investigate the position of the focal point, we computed longitudinal waves, generated by the SAWs and radiated into the fluid media from opposite sides of the microchannel, and the resultant pressure and velocity fields due to the interference and reflection of the longitudinal waves. Simulation results predict the existence of a focusing point which is in good agreement with our experimental observations. Compared with other 3D focusing techniques, this method is non-invasive, robust, energy-efficient, easy to implement, and applicable to nearly all types of microparticles.

Introduction

The ability to focus particles and cells into a confined region is important for many lab-on-a-chip applications such as flow cytometry,^{1–5} single molecule detection,^{6–9} protein folding,¹⁰ cell sorting^{11,12} and enzymatic kinetics.^{13–15} Focusing particles to a narrow stream, however, is not a trivial task. Due to the laminar nature of microfluidic flows, particles suspended in a fluid medium tend to follow the fluidic streamlines unless a lateral force moves them from their original paths. Hydrodynamic forces have been commonly used to manipulate streamlines to guide particles to a confined region.^{16–19} Sheath flows with high flow rates are often used to compress collections of particles for two-dimensional (2D) hydrodynamic focusing in planar microfluidic channels. However, for many applications, 2D hydrodynamic focusing is intrinsically problematic due to the lack of vertical focusing. For example, when using 2D hydrodynamic focusing for flow cytometry, cell velocity variation in

the vertical direction causes difficulties for cell sorting, and two or more cells may enter optical interrogation region at the same time.²⁰ In hydrodynamic focusing-based laminar mixers, flow velocity variations of the focused enzymes or chemical species in the vertical direction may result in different reaction times across the depth of the channel, which would make it extremely difficult to extract meaningful information about the reaction kinetics.¹⁴ The inherent limitations of 2D hydrodynamic focusing call for the development of three-dimensional (3D) focusing, in which the stream of particles is focused both horizontally and vertically.

To date, a few microfabricated 3D hydrodynamic focusing devices have been reported.^{16–23} However, in many of these 3D focusing devices the introduction of excessive sheath solutions causes sample dilution and dispersion, which is not desirable for many applications. Moreover, most of these devices require the complicated construction of multi-layer channels, which are difficult to fabricate using conventional soft lithographic techniques. Sheathless 3D hydrodynamic focusing can also be achieved using inertial microfluidics. This technique requires relatively high flow rates and long channels in order to focus the particles.²⁴

Alternative methods that have been utilized to demonstrate particle focusing in microfluidic channels are electroosmosis,^{25–34} dielectrophoresis (DEP),^{33–37} magnetophoresis,^{38–40} and acoustics.^{41–44} The acoustic-based methods appear to be ideal for on-chip microparticle manipulation because they are non-invasive, applicable to virtually all microparticles, and do not require sheath solutions.^{12,45–52} Standing acoustic waves have been used for particle focusing *via* implementation of piezoelectric transducers. Particles exposed to standing acoustic waves tend to

^aDepartment of Engineering Science and Mechanics, The Pennsylvania State University, University Park, PA, 16802, USA. E-mail: junhuang@psu.edu; Fax: +1 814-865-9974; Tel: +1 814-863-4209

^bThe DOW Chemical Company, Spring House Technology Center, Spring House, PA, 19477, USA

^cDepartment of Mechanical and Nuclear Engineering, The Pennsylvania State University, University Park, PA, 16802, USA

^dDepartment of Mechanical, Industrial, and Manufacturing Engineering, Oregon State University, Corvallis, OR, 97331, USA

[†] Electronic supplementary information (ESI) available: (1) Real-time video of fluorescent polystyrene beads focusing inside a microchannel; and (2) detailed information on device fabrication and simulation. See DOI: 10.1039/c1lc20042a

move towards nodal points. Although standing bulk acoustic waves (SBAWs) based techniques have shown promising results,^{53,54} their non-planar structures and complex fabrication processes make it challenging to integrate them with other planar lab-on-a-chip components. Previously, we introduced a 2D particle focusing technique using standing surface acoustic waves (SSAWs).⁴⁷ A PDMS microchannel was aligned and bonded between two parallel interdigital transducers (IDTs). Upon the application of an RF signal to the IDTs, a SSAW was generated and the suspended particles were focused to pressure nodes located, by design, in the middle of the microchannel width. Thus, 2D particle focusing was observed.⁴⁷

In this work, through experimental and computational studies, we demonstrate that utilizing the same SSAW method, 3D particle focusing in a continuously flowing microchannel can be achieved. In our 3D focusing device, longitudinal acoustic waves were radiated into the fluid media from the propagating surface acoustic waves (SAWs). The interference between these longitudinal waves and their reflections from the channel walls formed a standing acoustic wave field in the microchannel with a pressure node in the middle. Once the particles move towards the pressure nodal plane (2D focusing), they tend to aggregate at the maximum kinetic energy points within that plane (focusing in the vertical direction). Hence, suspended particles are focused in both the horizontal and vertical directions. This acoustic force-based 3D focusing technique is non-invasive, energy-efficient, applicable to virtually any microparticle, and easy to fabricate and implement. Utilizing this method, microparticles suspended in liquid media can be focused to a predesigned location, regardless of particle properties. Manipulation of various particle sizes and different cell types has been discussed in our previous studies.^{12,49} Unlike hydrodynamic focusing techniques, this SSAW focusing method does not require fluid inputs with high flow rates and is free from the particle dispersion problem. The high energy efficiency of our system stems from the fact that the acoustic energy is mainly confined to the surface of the substrate and dissipates weakly along the propagation line.⁵⁵

Experimental study

Device fabrication and experimental setup

Fig. 1a shows the device used in our study. Two sets of IDTs with a period of 100 μm and electrode width of 25 μm were arranged parallel to each other on a 128° Y-cut LiNbO_3 substrate. The IDTs were formed by e-beam evaporation of Ti (50 \AA , adhesive layer) and Au (800 \AA) followed by a lift-off process. A PDMS microchannel with 50 μm width and 100 μm height was fabricated by standard soft lithography and mold-replica techniques.⁵⁶ The PDMS microchannel was then aligned with the IDTs and bonded on the LiNbO_3 substrate such that a pressure node of the SSAW was located in the middle of the channel width. The bonding regions were treated with oxygen plasma to enhance the bonding between the PDMS channel and the LiNbO_3 substrate. To generate continuous flow, a syringe pump (KDS 210, KD scientific, Holliston, MA) was used.

To visualize the focused microparticles when the SSAW was generated, the experimental apparatus was mounted on the stage of an inverted microscope (Nikon TE2000U). A fluorescent

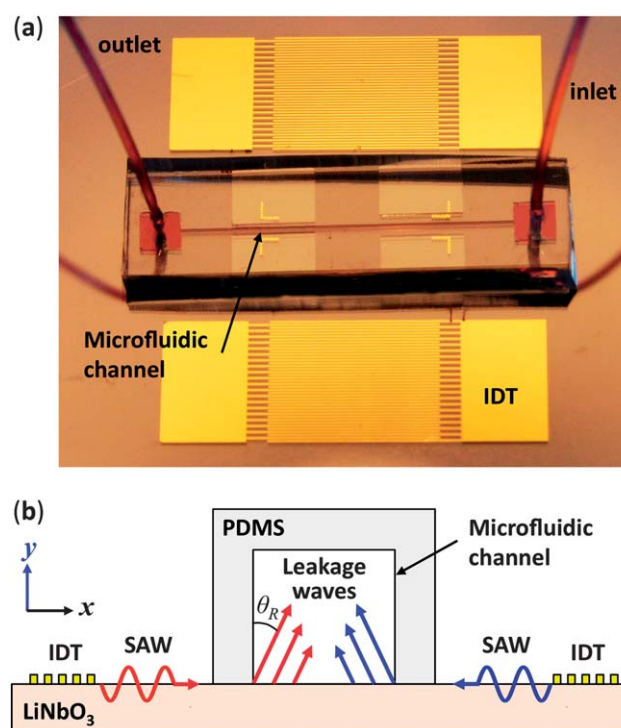


Fig. 1 (a) A photograph of the experimental apparatus is shown including a PDMS microchannel in between a pair of parallel IDTs. (b) A cross-section schematic of the microchannel and IDTs used to generate two SAWs travelling in the opposite direction. The leakage waves are radiated into the liquid phase under the Rayleigh angle (drawings are not in scale).

(dragon green) polystyrene bead (1.9 μm) solution was injected into the microchannel using the syringe pump. An RF signal generator (Agilent E4422B) produced an AC signal that was augmented by a power amplifier (Amplifier Research 100A250A). The amplified signal was equally partitioned into two separate signals, and applied to the two IDTs for SAW generation. The applied AC signal was set to 38.2 MHz, the excitation frequency for SAWs (Rayleigh mode) on LiNbO_3 , and the applied power was set to 24 dBm (~ 250 mW).

While particle behavior in the lateral (x - z plane) direction can be conveniently visualized through the microscope, monitoring the microparticle distribution across the channel height (y -direction) presents a significant challenge. To address this challenge, a triangular 45 degree prism was placed adjacent to the sidewall of the microchannel to visualize the y - z plane. As seen in Fig. 2a, the excitation light, coming from the bottom of the microscope stage into the triangular prism, was bent in the lateral direction toward the travelling particles in the microchannel. The excited microparticles emit fluorescent light that was reflected through the prism into the microscope to be recorded for analysis. Additionally, a CCD camera was connected to the microscope to capture images and real-time videos of our 3D focusing technique.

Experimental results

As discussed in the previous section, in order to observe focusing in the vertical direction, a prism was positioned next to the

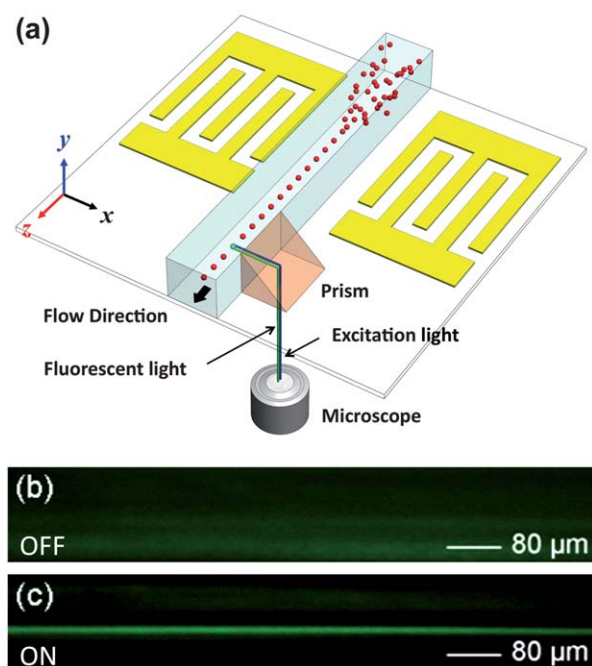


Fig. 2 (a) Schematic of the experimental setup for monitoring the particle behavior in the vertical direction (y -direction): a 45° prism adjacent to the channel was used to bend the excitation/fluorescent light for observation of particle migration in the y -direction. Recorded side view fluorescent images (b) before and (c) after the SSAW was generated.

PDMS channel sidewall. When the particles passed through the microchannel section adjacent to the prism at a flow rate of $7 \mu\text{L min}^{-1}$, their movement in the vertical direction (y - z plane) was captured through the prism using a CCD camera. As shown in Fig. 2b, when the RF signal is off and no SAW is generated, the distribution of the fluorescent particles across the microchannel is random. When the RF is switched on, the particles experience the acoustic radiation forces from the SAW-induced longitudinal-mode leakage waves in the microchannel. As a result, they are focused to a balance line, located about $42 \mu\text{m}$ above the bottom of the channel (Fig. 2c). Further details on the focusing mechanism are discussed in the theoretical section of this article.

Alternatively, we can confirm the 3D focusing using the recorded top-view images (Fig. 3). Compared to the previous results in Fig. 2, the flow rates for the top-view imaging results were reduced by an order of magnitude to $0.7 \mu\text{L min}^{-1}$. The images were taken from a fixed camera position over a period of 2 s to track the redistribution of particles upon SSAW generation. At $t = 0$, the RF signal was off, and the distribution of the particles was random in both lateral and vertical directions. Note that the particles out of the focal plane appear blurry and large. At $t = 0.1$ s, the SSAW was generated and the particles started to redistribute in the lateral and vertical directions. The yellow dotted contours show the snapshots of three particles when they redistribute in the lateral direction (x - z plane). As shown in different time snapshots, the acoustic radiation forces drove these particles to the pressure node of the SSAW located in the middle of the channel along the x -direction. The white dotted contours illustrate focusing in the vertical direction (y -direction): the particles out of the focal plane of the microscope, which appear large and blurry, were gradually driven to the focal plane

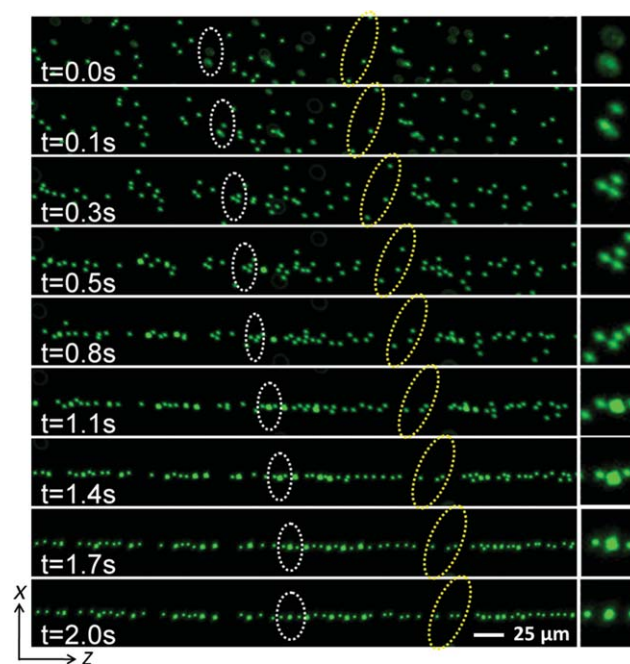


Fig. 3 Top-view images of the fluorescent particles recorded at different time snapshots. Particles are randomly distributed in the channel before the RF power is on ($t = 0$). After the RF signal is applied and the SSAW is generated, particles are focused laterally and vertically. The yellow dotted contours show three particles that are driven to the center of the channel (pressure nodal plane). The white dotted contours illustrate focusing in the vertical direction; these contours are enlarged on the right-side column. The three particles are out of focus before the signal is applied. When SSAW is generated, they start to migrate to the focal plane of the optical apparatus, implying migration in the y -direction (vertical direction).

of the microscope and aligned in the middle of the channel. The enlarged view of the selected particles in white contours is shown on the right-side column in Fig. 3. The duration of the entire focusing process is about 2 s, indicating the speed and efficiency of this focusing mechanism. It should be noted that a power less than 250 mW was used in this experiment in order to reduce the focusing speed to capture clear images. Reliable reversibility can be achieved by simply turning the SSAW on and off. After passing through the SSAW working region, the microparticles remain focused due to properties of laminar flow and large Peclet number.

Theoretical and computational study

In order to understand the working principle of the SSAW-based 3D focusing and investigate the position of the focal point, we performed simulations using MATLAB. The propagating SAW (Rayleigh mode) from each IDT with amplitude normal to the substrate surface is partially absorbed by the fluid. Due to this energy absorption, a finite pressure difference is generated in the fluid between the peaks of the wave. The pressure difference above the surface of the substrate leads to the generation of a longitudinal sound wave in the liquid. This acoustic energy leakage into the liquid causes an exponential

decay in the propagating SAW power. The leakage rate can be calculated as,⁵⁷

$$\alpha_0 = \frac{v_R z_w f_s}{v_S z_S \cos(\theta_R)}, \quad (1)$$

where v_R , v_S , z_w and z_S are Rayleigh-wave velocity, shear-wave velocity, impedance of water, and shear-wave impedance of the substrate, respectively. f_s is a dimensionless parameter of the substrate.⁵⁷ Because of the difference between the velocity of sound in the fluid and substrate, longitudinal waves are radiated into the fluid at an angle θ_R , known as the Rayleigh angle, which is determined by the ratio of speed of sound in liquid to the speed of sound in solid given by the Snell's law,^{57,58}

$$\sin(\theta_R) = \frac{v_w}{v_R}, \quad (2)$$

where v_w is the speed of sound in liquid.

We assume that when the propagating SAW from each IDT reach the microchannel, each point on the substrate generates a plane longitudinal wave propagating along the Rayleigh angle into the water, as illustrated in Fig. 1b. As the longitudinal waves travel through the water, their energy attenuates with distance due to viscosity and thermal effects. Reflection from the channel walls and interference between the longitudinal waves also affect acoustic fields in the channel and is accounted for in the simulation. The attenuation and reflection coefficients used in the simulations are provided in the ESI†. Fig. 4a presents a time snapshot of the displacement field of a longitudinal wave in the microchannel radiated from a SAW propagating in the positive x -direction. The other IDT generates a SAW travelling in the opposite direction, *i.e.*, negative x -direction (Fig. 4b). The arrows denote the local displacement magnitude and direction at a particular time. Both longitudinal waves enter the liquid under an angle of diffraction, θ_R , calculated as 22.5° according to eqn (2) with $v_w = 1490 \text{ m s}^{-1}$ and $v_R = 3900 \text{ m s}^{-1}$. Note that interference of these two oppositely propagating SAWs leads to the formation of a SSAW on the substrate.

The resultant displacement field of these longitudinal waves generated by two oppositely propagating SAWs forms a standing wave along the x -direction in the cross-section of the microchannel. The corresponding pressure field of the combined displacement fields from Fig. 4a and b was simulated at two time snapshots with a time difference of half a period ($\tau/2$). These simulation results are shown in Fig. 4c and d. Due to the interference of the radiated and reflected longitudinal waves, the resultant pressure field is not uniform. The strong discontinuity in the pressure field in Fig. 4c and d is due to the destructive interference of the radiated longitudinal waves and their reflections from the channel walls. During this time difference, the amplitude of the pressure in the y - z plane of the channel at $x = 25 \mu\text{m}$ remains zero (dashed line), while the pressure in the other analogous regions simply changes sign. These facts indicate that a pressure node exists in the middle plane of the channel ($x = 25 \mu\text{m}$), as denoted by the dashed lines in Fig. 4c and d.

The longitudinal waves induce pressure fluctuations in the liquid which, in turn, generate primary acoustic radiation forces. As a result of the radiation forces, suspended particles in the liquid aggregate at pressure nodes or anti-nodes depending on the relative density and compressibility of the particles and fluid

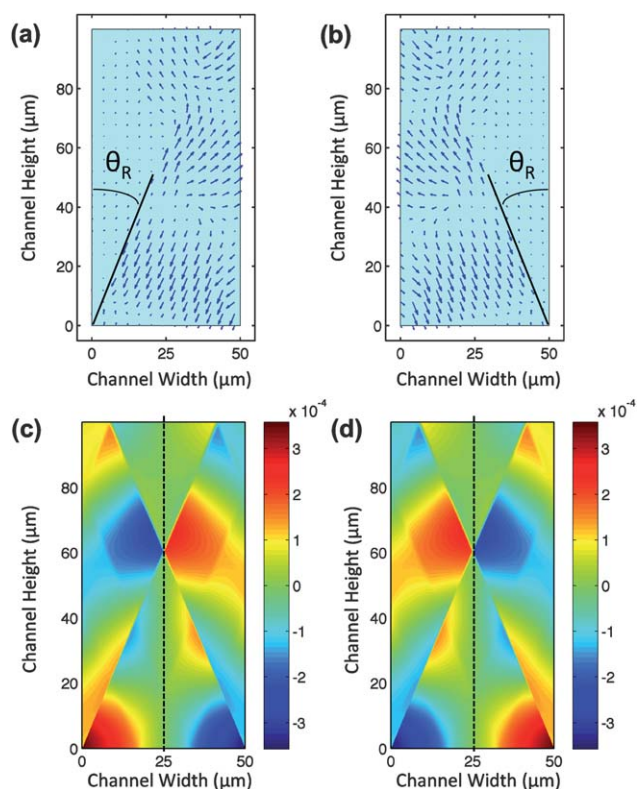


Fig. 4 Time snapshots of displacement of the longitudinal-mode leakage wave from a SAW propagating in (a) the positive x -direction and (b) the negative x -direction. Resultant pressure field of the generated SSAW due to the penetration of two SAWs from opposite directions is shown in the cross-section of the channel at (c) $t = t_0$ and (d) $t = t_0 + \tau/2$. Resultant pressure field distribution confirms the existence of a pressure nodal plane in the middle of the channel, as denoted by the dotted lines.

media.⁵⁹ As shown in Fig. 4c and d, a pressure node exists in the middle of the microchannel once the SSAW is generated. Eqn (3) gives the expression for the primary radiation forces F_{ax} ,

$$F_{ax} = -\left(\frac{\pi\rho_0^2 V_c \beta_w}{2\lambda}\right)\varphi(\beta, \rho)\sin(2kx), \quad (3)$$

where P_0 and V_c are the acoustic pressure and particle volume, respectively; λ is the wavelength; β is compressibility; ρ is density; and φ , the acoustic contrast factor, indicates whether particles aggregate at pressure nodes (positive φ) or pressure anti-nodes (negative φ).⁵⁹

$$\varphi(\beta, \rho) = \frac{5\rho_c - 2\rho_w}{2\rho_c + \rho_w} - \frac{\beta_c}{\beta_w}, \quad (4)$$

where subscript c and w stand for particle and fluid, respectively. In our experiments, we used fluorescent polystyrene beads of a positive φ . Hence, the polystyrene particles in the microchannel move towards the pressure nodal plane. The constant values in eqn (3) and (4) can be found in ref. 60.

In our SSAW-based device, standing waves have a non-uniform acoustic field distribution in the vertical direction (*i.e.*, y -direction), owing to a number of reasons such as near-field effects,⁶¹ source inhomogeneity,⁶² and energy density reduction towards the edges of localized axial field.⁶³ This inhomogeneous acoustic energy distribution in the vertical direction generates the

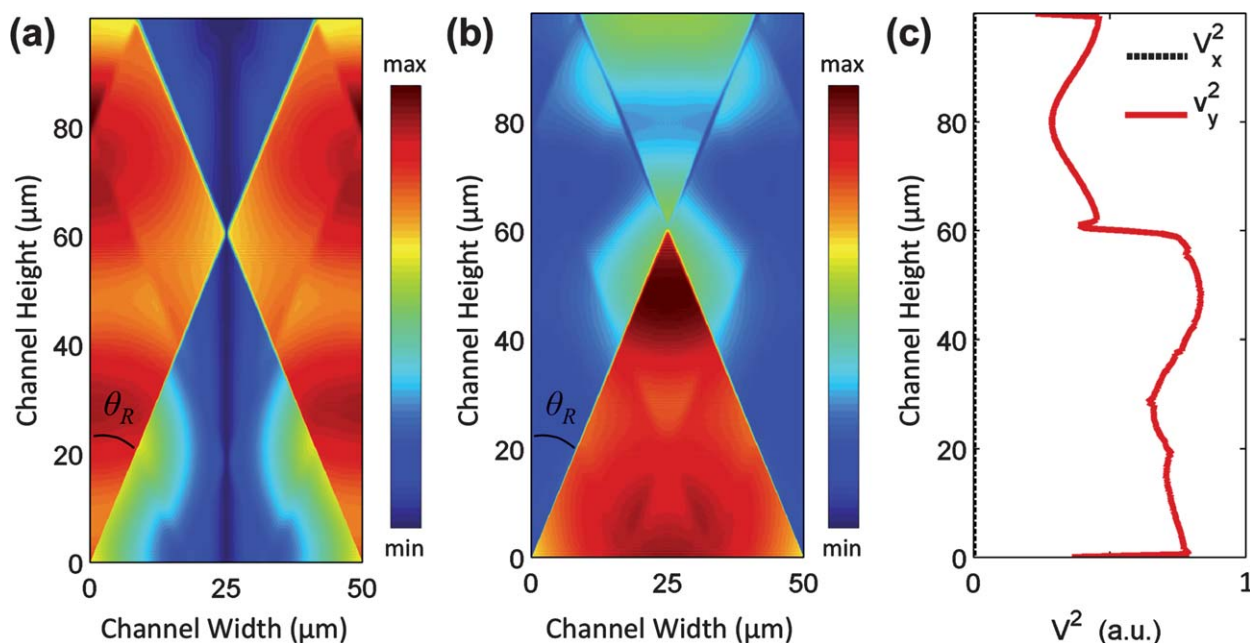


Fig. 5 Time-averaged velocity squared field in the (a) x -direction (V_x^2) and (b) y -direction (V_y^2) is shown. (c) Time-averaged velocity squared in the x -direction (V_x^2) and y -direction (V_y^2) within the middle plane ($x = 25 \mu\text{m}$) is plotted.

transverse primary radiation forces.⁵⁵ Once the particles are moved, by the axial primary radiation forces, to the pressure nodal (y - z) plane in the center of the microchannel, the transverse primary radiation forces move them to particular points with maximum acoustic kinetic energy within the nodal plane. These points are referred to by Schram as “acoustic hot spots”.⁶⁴ Note that focusing of particles is due to the balance of axial and transverse primary radiation forces; however, the working mechanisms of these two forces are different. Axial primary forces are stronger, so they first push the particles to the pressure nodal plane. Then the weaker transverse force, which depends on acoustic energy gradient, forces the particles to maximum kinetic energy point. Please refer to ESI† for more details.

Because the time-averaged kinetic energy KE is proportional to the square of velocity (V^2),⁶⁰

$$\text{KE} = \frac{\rho_w V^2}{2}, \quad (5)$$

the distribution of the velocity field is required in order to find the maximum kinetic energy point(s) within the pressure nodal plane. Fig. 5a and b demonstrate the time-averaged velocity squared field in the x and y directions, respectively. Note that we are merely interested in the square of the velocity’s magnitude within the pressure nodal plane. Fig. 5c shows the time-averaged distribution of velocity squared in x and y directions within the pressure nodal plane. The discontinuities near $y = 20 \mu\text{m}$ and $y = 60 \mu\text{m}$ are due to destructive interference of the longitudinal waves. As shown in Fig. 5a, the magnitude of the time-averaged velocity squared in the x -direction in the nodal plane is zero (black dotted contour in Fig. 5c). Hence, the magnitude of the time-averaged velocity squared is equal to the time-averaged velocity squared in the y -direction (V_y^2), represented by the red solid curve. The local maximum of the V_y^2 contour, which from eqn (5) is also the local maximum kinetic energy, is

approximately at $y = 46 \mu\text{m}$. Thus, after the particles are focused to the middle of the microchannel due to the axial primary radiation forces, transverse primary radiation forces push them to a point around $46 \mu\text{m}$ above the bottom of the channel: the “acoustic hot spot.” It is worth mentioning that the position of the focal point is highly dependent on the channel design. The width of the channel is determined by the applied frequency. Therefore, after fixing the width, channel height can be used as a design parameter to change the position of the focused particles in the vertical direction (y -direction). Overall, increasing the channel height decreases the normalized focusing point. Please refer to ESI† for more details.

The minor discrepancy between experimental ($y = 42 \mu\text{m}$) and computational ($y = 46 \mu\text{m}$) results can be attributed to several factors. The main factor is the longitudinal waves penetrating the microchannel from the bulk acoustic waves (BAWs) generated from IDTs that travel within the bulk of the piezoelectric substrate.^{65–68} Due to the complex nature of the transportation and attenuation of BAW energy and numerous interactions between the different travelling waves in the microchannel, this factor was not considered in our calculations. Another factor that could contribute to the discrepancy in the final focusing position is the secondary field forces.^{59,60} The resultant force is primarily attributed to the overall travelling forces, although the secondary forces do have minor, undetermined effects on the final balance point.

Conclusions

In conclusion, we demonstrate 3D continuous particle focusing in a microfluidic channel using SSAWs. Simulation results predict the existence and location of a focusing point, which is in good agreement with our experimental observations. Compared with many existing 3D particle focusing techniques,

our SSAW-based method is non-invasive, reversible, energy-efficient, easy to implement, and applicable to almost any microparticle. With these advantages, this method is expected to be valuable in many lab-on-a-chip applications.

Acknowledgements

The authors thank Brian Kiraly for the helpful discussion. This research was supported by NIH Director's New Innovator Award (1DP2OD007209-01), the National Science Foundation (0348149, 0824183, and 0801922), US Department of Agriculture (USDA/NRI), Air Force Office of Scientific Research (AFOSR), and the Penn State Center for Nanoscale Science (MRSEC). Components of this work were conducted at the Penn State node of the NSF-funded National Nanotechnology Infrastructure Network.

References

- 1 M. M. Wang, E. Tu, D. E. Raymond, J. M. Yang, H. Zhang, N. Hagen, B. Dees, E. M. Mercer, A. H. Forster, I. Kariv, P. J. Marchand and W. F. Butler, *Nat. Biotechnol.*, 2005, **23**, 83–87.
- 2 X. Mao, S.-C. S. Lin, C. Dong and T. J. Huang, *Lab Chip*, 2009, **9**, 1583–1589.
- 3 C. Simonnet and A. Groisman, *Anal. Chem.*, 2006, **78**, 5653–5663.
- 4 H. Yun, H. Bang, J. Min, C. Chung, J. K. Chang and D.-C. Han, *Lab Chip*, 2010, **10**, 3243–3254.
- 5 S. C. Hur, H. T. Kwong Tse and D. Di Carlo, *Lab Chip*, 2010, **10**, 274–280.
- 6 A. J. De Mello and J. B. Edel, *J. Appl. Phys.*, 2007, **101**, 084903.
- 7 M. Kim, D. J. Hwang, H. Jeon, K. Hiromatsu and C. P. Grigoropoulos, *Lab Chip*, 2009, **9**, 311–318.
- 8 T. H. Wang, Y. Peng, C. Zhang, P. K. Wong and C. M. Ho, *J. Am. Chem. Soc.*, 2005, **127**, 5354–5359.
- 9 C.-Y. Zhang, S.-Y. Chao and T. H. Wang, *Analyst*, 2005, **130**, 483–488.
- 10 Y. Gambin, C. Simonnet, V. VanDelinder, A. Deniz and A. Groisman, *Lab Chip*, 2010, **10**, 598–609.
- 11 T. Franke, S. Braunmüller, L. Schmid, A. Wixforth and D. A. Weitz, *Lab Chip*, 2010, **10**, 789–794.
- 12 J. Shi, H. Hua, Z. Stratton, Y. Huang and T. J. Huang, *Lab Chip*, 2009, **9**, 3354–3359.
- 13 J. B. Knight, A. Vishwanath, J. P. Brody and R. H. Austin, *Phys. Rev. Lett.*, 1998, **80**, 3863–3866.
- 14 L. Pollack, M. W. Tate, N. C. Darnton, J. B. Knight, S. M. Gruner, W. A. Eaton and R. H. Austin, *Proc. Natl. Acad. Sci. U. S. A.*, 1999, **96**, 10115–10117.
- 15 S. A. Pabit and S. J. Hagen, *Biophys. J.*, 2002, **83**, 2872–2878.
- 16 N. Sundararajan, M. S. Pio, L. P. Lee and A. A. Berlin, *J. Microelectromech. Syst.*, 2004, **13**, 559–609.
- 17 C. Simonnet and A. Groisman, *Appl. Phys. Lett.*, 2005, **87**, 114104.
- 18 R. Yang, D. L. Feedback and W. Wang, *Sens. Actuators, A*, 2005, **118**, 259–267.
- 19 C. C. Chang, Z. X. Huang and R. J. Yang, *J. Micromech. Microeng.*, 2007, **17**, 1479–1486.
- 20 S. Eyal and S. R. Quake, *Electrophoresis*, 2002, **23**, 2653–2657.
- 21 X. Mao, J. R. Waldeisen and T. J. Huang, *Lab Chip*, 2007, **7**, 1260–1262.
- 22 A. Terray and S. J. Hart, *Lab Chip*, 2010, **10**, 1729–1731.
- 23 J. Oakey, R. W. Applegate, E. Arellano, D. Di Carlo, S. W. Graves and M. Toner, *Anal. Chem.*, 2010, **82**, 3862–3867.
- 24 D. Di Carlo, D. Irimia, R. Tompkins and M. Toner, *Proc. Natl. Acad. Sci. U. S. A.*, 2007, **104**, 18892–18897.
- 25 A. Y. Fu, C. Spence, A. Scherer, F. H. Arnold and S. R. Quake, *Nat. Biotechnol.*, 1999, **17**, 1109–1111.
- 26 S. C. Jacobson and J. M. Ramsey, *Anal. Chem.*, 1997, **69**, 3212–3217.
- 27 D. P. Schrum, C. T. Culbertson, S. C. Jacobson and J. M. Ramsey, *Anal. Chem.*, 1999, **71**, 4173–4177.
- 28 P. K. Wong, T. H. Wang, J. H. Deval and C. M. Ho, *IEEE/ASME Trans. Mechatronics*, 2004, **9**, 366–376.
- 29 P. K. Wong, C. Y. Chen, T. H. Wang and C. H. Ho, *Anal. Chem.*, 2004, **76**, 6908–6914.
- 30 D. Erickson, X. Liu, R. Venditti, D. Li and U. J. Krull, *Anal. Chem.*, 2005, **77**, 4000–4007.
- 31 D. Erickson, X. Liu, U. Krull and D. Li, *Anal. Chem.*, 2004, **76**, 7269–7277.
- 32 A. J. Chung, D. Kim and D. Erickson, *Lab Chip*, 2008, **8**, 330–338.
- 33 H. Chu, I. Doh and Y. Cho, *Lab Chip*, 2009, **9**, 686–691.
- 34 T. Glawdel and C. L. Ren, *Encyclopaedia of Microfluidics and Nanofluidics*, Springer-Verlag Heidelberg, 2008, pp. 516–516.
- 35 D. Holmes, H. Morgan and N. Green, *Biosens. Bioelectron.*, 2006, **21**, 1621–1630.
- 36 L. Liang, S. Qian and X. Xuan, *J. Colloid Interface Sci.*, 2010, **350**, 377–379.
- 37 C. Yu, J. Vykoukal, D. Vykoukal, J. Schwartz, L. Shi and P. Gascoyne, *J. Microelectromech. Syst.*, 2005, **14**, 480–487.
- 38 C. Liu, T. Stakenborg, S. Peeters and L. Lagae, *J. Appl. Phys.*, 2009, **105**, 102014.
- 39 C. Liu, L. Lagae and G. Borghs, *Appl. Phys. Lett.*, 2007, **90**, 184109.
- 40 C. D. James, J. McClain, K. R. Pohl, N. Reuel, K. E. Achyuthan, C. J. Bourdon, K. Rahimian, P. C. Galambos, G. Ludwig and M. S. Derzon, *J. Micromech. Microeng.*, 2010, **20**, 045015.
- 41 A. Nilsson, F. Petersson, H. Jönsson and T. Laurell, *Lab Chip*, 2004, **4**, 131–135.
- 42 G. R. Goddard, C. K. Sanders, J. C. Martin, G. Kaduchak and S. W. Graves, *Anal. Chem.*, 2007, **79**, 8740–8746.
- 43 F. Petersson, A. Nilsson, C. Holm, H. Jönsson and T. Laurell, *Lab Chip*, 2005, **5**, 20–22.
- 44 T. Laurell, F. Petersson and A. Nilsson, *Chem. Soc. Rev.*, 2007, **36**, 492–506.
- 45 L. Kuznetsova and W. T. Coakley, *J. Acoust. Soc. Am.*, 2004, **116**, 1956–1966.
- 46 K. Yasuda, S. Umemura and K. Takeda, *Jpn. J. Appl. Phys.*, 1996, **1**, 3295–3299.
- 47 J. Shi, X. Mao, D. Ahmed, A. Colletti and T. J. Huang, *Lab Chip*, 2008, **8**, 221–223.
- 48 K. P. Kulkarni, S. H. Ramarathinam, J. Friend, L. Yeo, A. W. Purcell and P. Perlmutter, *Lab Chip*, 2010, **10**, 1518–1520.
- 49 J. Shi, D. Ahmed, X. Mao, S.-C. S. Lin, A. Lawit and T. J. Huang, *Lab Chip*, 2009, **9**, 2890–2895.
- 50 P. R. Rogers, J. R. Friend and L. Y. Yeo, *Lab Chip*, 2010, **10**, 2979–2985.
- 51 D. Ahmed, X. Mao, J. Shi, B. Krishna Juluri and T. J. Huang, *Lab Chip*, 2009, **9**, 2738–2741.
- 52 D. Ahmed, X. Mao, B. Krishna Juluri and T. J. Huang, *Microfluid. Nanofluid.*, 2009, **7**, 727–731.
- 53 F. Petersson, L. Aberg, A. M. Sward-Nilsson and T. Laurell, *Anal. Chem.*, 2007, **79**, 5117–5123.
- 54 G. Goddard, J. Martin, S. Graves and G. Kaduchak, *Cytometry, Part A*, 2006, **69**, 66–74.
- 55 B. A. Auld, in *Acoustic Fields and Waves in Solids*, Robert E. Krieger, 1990, vol. 2, pp. 88–94.
- 56 Y. Xia and M. Whitesides, *Langmuir*, 1997, **13**, 2059–2067.
- 57 C.-H. Chou, B. T. Khuri-Yakub and G. S. Kino, *IEEE Trans. Ultrason. Ferroelectrics Freq. Contr.*, 1988, **35**, 464–469.
- 58 Z. Guttenberg, A. Rathgeber, S. Keller, J. O. Rädler, A. Wixforth, M. Kostur, M. Schindler and P. Talkner, *Phys. Rev. E: Stat., Nonlinear, Soft Matter Phys.*, 2004, **70**, 056311.
- 59 M. Hill and N. R. Harris, in *Microfluidic Technologies for Miniaturized Analysis Systems: Ultrasonic Particle Manipulation*, Springer, 2007, pp. 357–392.
- 60 S. M. Woodside, B. D. Bowen and J. M. Piret, *AIChE J.*, 1997, **43**, 1727–1736.
- 61 T. Lilliehorn, U. Simu, M. Nilsson, M. Almqvist, T. Stepinski, T. Laurell, J. Nilsson and S. Johansson, *Ultrasonics*, 2005, **43**, 293–303.
- 62 M. Groschl, *Acustica*, 1998, **84**, 432–447.
- 63 D. Bazou, G. A. Foster, J. R. Ralphs and W. T. Coakley, *Mol. Membr. Biol.*, 2005, **22**, 229–240.
- 64 C. J. Schram, in *Advances in Sonochemistry: Manipulation of Particles in an Acoustic Field*, ed. T. J. Mason, Elsevier, 1991, pp. 293–322.
- 65 C. K. Campbell, in *Surface Acoustic Wave Devices for Mobile and Wireless Communications*, Academic Press, 1998, pp. 56–58.
- 66 J. Shi, S.-C. S. Lin and T. J. Huang, *Appl. Phys. Lett.*, 2008, **92**, 111901.
- 67 S.-C. S. Lin and T. J. Huang, *J. Appl. Phys.*, 2009, **106**, 053529.
- 68 S.-C. S. Lin, T. J. Huang, J.-H. Sun and T.-T. Wu, *Phys. Rev. B: Condens. Matter Mater. Phys.*, 2009, **79**, 094302.